INORGANIC CHEMISTRY FRONTIERS

CHINESE CHEMICAL SOCIETY

ROYAL SOCIETY OF CHEMISTRY

RESEARCH ARTICLE

View Article Online
View Journal | View Issue

Cite this: *Inorg. Chem. Front.*, 2022, **9**, 2697

Kinetic separation of C_2H_6/C_2H_4 in a cage-interconnected metal–organic framework: an interaction-screening mechanism†

Mo Xie, Zhou Lu, ‡ Weigang Lu * and Dan Li *

Received 2nd March 2022,
Accepted 12th April 2022

DOI: 10.1039/d2qi00465h

rsc.li/frontiers-inorganic

Kinetic-based adsorptive separation is deemed as an energy-efficient approach for gas purification, yet its underlying mechanism is difficult to justify. Herein, we propose an intriguing interaction-screening mechanism with a cage-interconnected metal–organic framework (**JNU-2**) as a model *via* a multi-scale theoretical approach. Grand Canonical Monte Carlo (GCMC) simulations establish gas diffusion channels with the calculated C_2H_4 and C_2H_6 adsorptions comparable to the experimental ones. Molecular dynamic (MD) simulations reveal single-molecule passages along the diffusion channel and that the probability of C_2H_6 diffusing into the passage is nine times higher than that of C_2H_4. Density functional theory (DFT) calculations further confirm an overall preferential interaction with C_2H_6 passing through the single-molecule passage. This work has successfully demonstrated a theoretical methodology of multi-scale simulations and depicted a rarely observed interaction-screening mechanism in **JNU-2** that corroborates its balanced adsorption capacity and C_2H_6/C_2H_4 adsorption selectivity. Such a methodology should be applicable to other well-defined structures for a better understanding of their gas adsorption/separation behaviours.

Introduction

Metal–organic frameworks (MOFs), a class of advanced nanoporous materials, show great application potential in the field of gas adsorption and separation due to their tunable pore sizes, large accessible surface areas, and chemical modifiability.[1–3] MOFs are constructed through metal clusters/metal ions and organic linkers, which facilitate the introduction of desired structural elements targeting specific guest molecules.[4] Taking light hydrocarbon separation as an example, suitable surface functionalization and matching pore size could selectively amplify the host–guest interaction, leading to excellent separation efficiency.[5–9]

Clarifying gas adsorption behaviours in the existing MOFs would be of great benefit for the further design and applications of new MOFs, such as gas storage and purification.[10] Studies on thermodynamics-dominant gas separation of MOF materials have been developed maturely by combining the experimental data and theoretical calculations. MOF-74 is one of the representatives with open metal sites (OMSs) to show excellent gas adsorption and separation behaviours by thermodynamic interactions, in which the OMSs provide strong binding sites to unsaturated C–C bonds and thus produce higher selectivity of olefins/alkynes over alkanes.[11,12] Kinetic sieving is another efficient strategy that has been widely applied owing to its excellent separation capability and easy desorption.[13,14] The classic size-exclusion mechanism of kinetic sieving leads to selective adsorption of the small-sized one but fails to explain the reversed selectivity. In contrast to enormous experimental results and evidence, theoretical simulation has witnessed development lag likely due to the difficulties in determining the precise locations of loaded gas molecules and predicting the gas diffusion process. Meanwhile, traditional static models with loaded gas molecules, some from X-ray diffraction determination, are not conducive to revealing of a kinetic-based adsorption and selectivity mechanism.[15,16] In this regard, molecular dynamic (MD) simulation in combination with Grand Canonical Monte Carlo (GCMC) is a powerful tool to probe the dynamic behaviours of gas molecules in MOFs.[17–19] A comprehensive multi-scale simulation would be essential for painting a full picture of the gas adsorption behaviour, locally and globally, kinetically and thermodynamically.

Recently, our research group reported a microporous MOF (JNU-2) featuring large adsorption capacity and high C_2H_6/C_2H_4 selectivity.[20] Single-component equilibrium adsorption

---

College of Chemistry and Materials Science, Guangdong Provincial Key Laboratory of Functional Supramolecular Coordination Materials and Applications, Jinan University, Guangzhou, Guangdong 510632, People's Republic of China. E-mail: weiganglu@jnu.edu.cn, danli@jnu.edu.cn

† Electronic supplementary information (ESI) available. See DOI: **https://doi.org/10.1039/d2qi00465h**

‡ Present address: Department of Chemistry, University of North Texas, Denton, Texas 76203, USA.

and binding enthalpies for C_2H_6 and C_2H_4 indicate the similarity between their absorption behaviours, but the mixed-gas breakthrough experiments reveal an excellent C_2H_6/C_2H_4 separation (Fig. S1 and S2†). It was suggested that kinetics might play a crucial part in this, while this C_2H_6-favoured adsorption did not conform to the classic molecular sieving mechanism. Herein, we carried out a multi-scale simulation study on **JNU-2** to clarify the underlying kinetic mechanism for C_2H_6/C_2H_4 separation. GCMC simulations suggest that the largest cage (**Cage C**) is not accessible to C_2H_6 and C_2H_4 due to the small size of the opening windows. MD simulations further confirm that **channel I** connecting the two smaller cages (**Cage A** and **Cage B**) is the only gas diffusion pathway and **Cage A** is a single-molecule passage, while **Cage B** functions as a gas adsorption and storage chamber. DFT calculations demonstrate a negligible thermodynamic effect of **Cage B** on C_2H_6 and C_2H_4 but an overall more favourable interaction energy pathway for C_2H_6 diffusion through **Cage A.** The above multi-scale simulations and calculations enable us to establish an interaction-screening-based kinetic separation mechanism in **JNU-2** for C_2H_6/C_2H_4 separation. This work demonstrates a generalizable theoretical methodology for the in-depth understanding of gas adsorptions and separations in MOF-based materials.

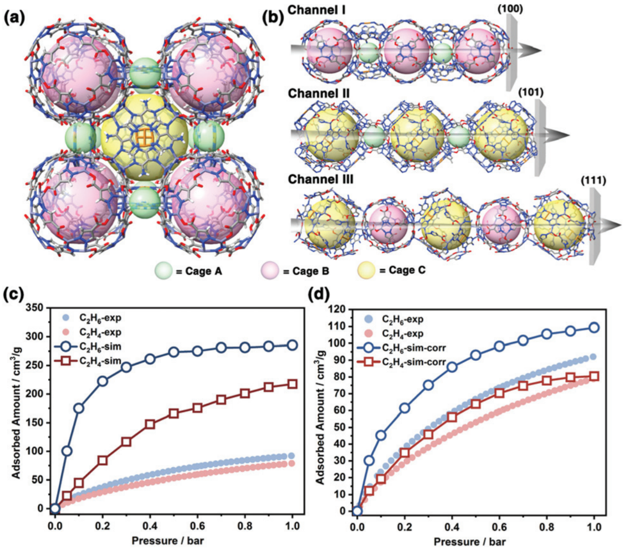

Fig. 1 (a) An orthogonal stacking of the three cages in the crystal structure of **JNU-2**, where **Cage A**, **B**, and **C** are highlighted in coloured spheres. H atoms are omitted for clarity. Colour representation: gold, Cu; dark blue, Zn; blue, N; grey, C; red, O. (b) Three possible gas diffusion channels in **JNU-2**. (c) GCMC simulated adsorption isotherms of C_2H_6 and C_2H_4 in reference to the experimental data. (d) The corrected GCMC simulated adsorption isotherms of C_2H_6 and C_2H_4 in reference to the experimental data.

Results and discussion

The desired material **JNU-2** was reproduced by previous reports; adsorption enthalpy (Q_{st}) of C_2H_6 and C_2H_4 in **JNU-2** is provided in Fig. S1† and breakthrough curves for the C_2H_6/C_2H_4 (10/90) mixture through **JNU-2** are shown in Fig. S2†. For discussion convenience, the three cage-like cavities in the crystal structure of **JNU-2**, from small to large, are referred to as **Cage A**, **B**, and **C** (Fig. 1a). Each two of them are linearly interconnected into one-dimensional channels in the directions perpendicular to the (100), (101), and (111) crystal planes, labelled as **Channel I**, **II**, and **III**, respectively (Fig. 1b).

GCMC simulation

GCMC simulation is a powerful tool to study gas adsorption in porous materials including MOFs. It can provide not only adsorption isotherms but also gas distribution statistics inside the frameworks accordingly, allowing us to locate the strong adsorption sites. In this manner, we carried out GCMC simulations of the adsorption of C_2H_6 and C_2H_4 on **JNU-2**, respectively. The adsorption isotherms (Fig. 1c) show that the simulated C_2H_6 adsorption is higher than that of C_2H_4 at all pressure points, which is consistent with the experimental data. However, a huge discrepancy is observed between the simulation and experiment for both C_2H_6 and C_2H_4, suggesting that the simulations do not fully reflect their real adsorption situations.

To figure out the reason for the simulation/experiment discrepancy, the simulated gas distribution of C_2H_6 and C_2H_4 inside **JNU-2** was analyzed. The adsorptions of C_2H_6 and C_2H_4 appear quite similar based on their distribution density maps; both are evenly distributed in all three cavities (**Cage A**, **B**, and **C**) (Fig. S3†), suggesting that the discrepancy is not caused by an overestimation of adsorption sites. We subsequently calculated the adsorption isotherms by replacing the UFF/TraPPE force field with the Dreiding[21]/OPLS-AA[22] force field and using the Gasteiger charge in simulations. As shown in Fig. S4,† the Dreiding/OPLS-AA simulation results are almost the same as before. Thus, we can rule out that the simulation parameters are the cause of the simulation/experiment discrepancy. **JNU-2** is a rigid framework as demonstrated in our experimental report,[20] in which the flexibility should not be the reason for the discrepancy either. A further look into the GCMC simulations showed that the insertion, translation, and rotation of the adsorbates inside the framework were allowed, but ignoring their kinetic behaviors could overestimate the adsorption in some cavities with small apertures in the above GCMC simulations. Therefore, we speculated that C_2H_6 and C_2H_4 molecules may not be able to enter some of the cavities in **JNU-2**, which was overlooked in adsorption simulations. The gas accessibility to the three cages was examined through the volume and limiting diameter analysis. The probe radius used in the calculations was set to be 2.8 Å, leading to non-smooth spherical accessible dimensions with slight overflows, which were further estimated to be 133 Å^3, 1873 Å^3, and 3134 Å^3 for **Cage A**, **B**, and **C**, respectively (Fig. 2). Every two of them are interconnected through a window (aperture), resulting in a total of three different kinds of windows in **JNU-2.** A cross-section can be obtained if we cut a plane at the narrowest part

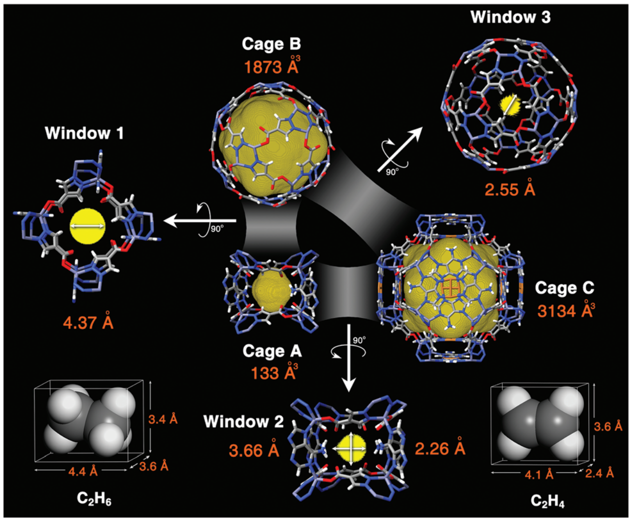

Fig. 2 The calculated volume (yellow sphere) and window size of the three cages along with the size of gas molecules (orange value). **Window 1** connects **Cage A** and **Cage B**, **Window 2** connects **Cage B** and **Cage C**, and **Window 3** connects **Cage A** and **Cage C**.

of the window, and the size of the thus-obtained cross-section should be the limiting size of the window. By performing this, we can see that **Window 1** has a round cross-section with a diameter of 4.37 Å, **Window 2** has a triangular cross-section with a maximum distance of 2.55 Å, and **Window 3** has an elliptical cross-section with maximum and minimum diameters of 3.66 Å and 2.26 Å, respectively. Considering the kinetic diameters of C_2H_6 and C_2H_4 molecules, it seems that **Window 1** serves as the only passable aperture for both gas molecules. The other two windows, both connecting to **Cage C**, are too small to allow either of the gas molecules to pass through, indicating that **Cage C** should be inaccessible to C_2H_6 and C_2H_4.

To correct the GCMC simulations, we performed the GCMC simulations using another commonly-used software RASPA 2.0[23] by employing the same force field and atomic charge calculation method (UFF/TraPPE, Q_{eq} charge). To block the adsorption in **Cage C**, a solid sphere was placed at the center of **Cage C** and its radius was set to 8 nm; the schematic diagram of the blocking sphere in **JNU-2** is shown in Fig. S5.† The RASPA-simulated adsorption (Fig. 1d) after correction is in good agreement with the experimental data. The slightly higher uptake for both C_2H_6 and C_2H_4 could be attributed to the irregularity of **Cage C** and it is not well represented by the blocking sphere in RASPA calculations. Overall, the corrected adsorption is consistent with the experimental data, which strongly supports our assumption that **Cage C** is inaccessible to C_2H_6 and C_2H_4.

MD simulation

To study the dynamic adsorption behavior of C_2H_6/C_2H_4 inside **JNU-2**, MD simulations were conducted. Owing to the symmetry and rigidity of **JNU-2**, the directions of three possible gas diffusion pathways (**Channel I**, **Channel II**, and **Channel III**) are perpendicular to the (100), (110), and (111) crystal planes of **JNU-2**. We accordingly set the (100), (110), or (111) crystal face from the unit cell of **JNU-2** as the interface with the gas phase, so that the gas molecules can move along the directions of three channels. As shown in Fig. 3, all gas molecules diffused into the cages of **Channel I** after 20 ns, and the rigidity of the framework was well maintained. However, only a negligible amount of gas molecules diffused through the first cage of **Channel II** or **Channel III**, further verifying our assumption that **Cage C** was not accessible to either C_2H_4 or C_2H_6. The snapshots of gas distribution and concentration profiles of C_2H_4 and C_2H_6 in the *z*-axis direction and *x*/*y*-axis direction within the 20 ns simulations were further tracked and are

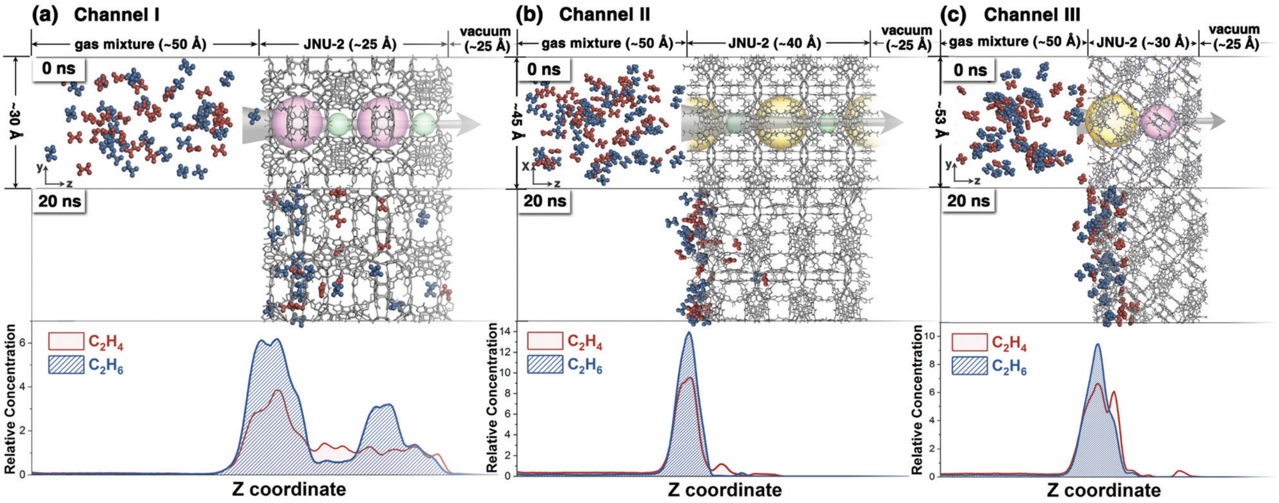

Fig. 3 MD simulation of the C_2H_4/C_2H_6 (1 : 1) mixture passing through (a) **Channel I**, (b) **Channel II**, and (c) **Channel III** of **JNU-2** along the *z*-axis. Top: snapshots of the gas distribution at the initial (0 ns) and final (20 ns) stages. Bottom: gas concentration profiles of C_2H_6 and C_2H_4 along the *z* coordinate. H atoms in the models are omitted and the C_2H_6 and C_2H_4 molecules are highlighted in lake blue and rose red for clarity.

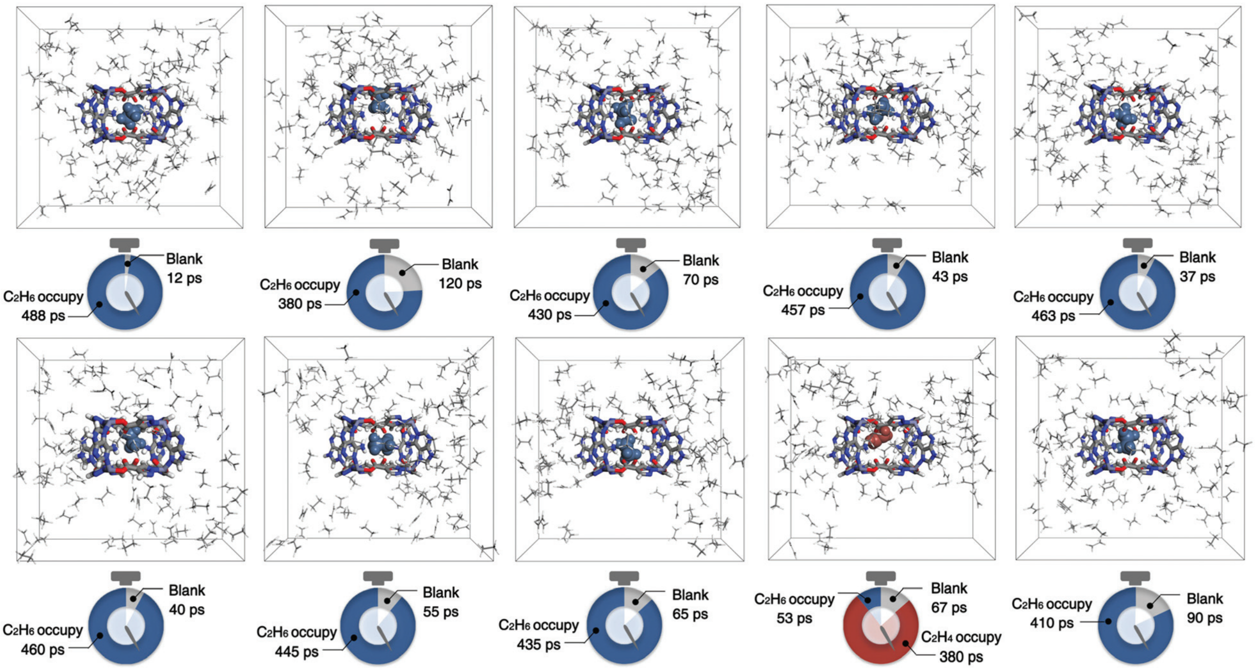

Fig. 4 Snapshots of gas molecules entering into **Cage A** in 10 parallel 500 ps MD simulations in a box (30 Å × 30 Å × 30 Å) filled with a C_2H_6/C_2H_4 (1 : 1) mixture. The C_2H_6 and C_2H_4 molecules entering **Cage A** are coloured in lake blue and rose red respectively. The corresponding time bar represents the gas residence time in **Cage A** within 500 ps.

shown in Fig. 3 and Fig. S6,† respectively. Interestingly, the concentrations of both gas molecules in **Cage A** are lower than 2 from the *yz* view (Fig. 3a), and 1.2 from the *xz* and *xy* view (Fig. S6†). Subtracting those being close to interconnected open pores, the number of gas molecules inside **Cage A** should be less than or equal to 1, suggesting that **Cage A** can only accommodate one gas molecule. It is worth noting that there are partially opened cavities on the interface. Without restricting the direction of gas diffusion, only a few gas molecules were observed passing through the interface and entering into the framework layer. This further confirms that **Channel I** is the only gas diffusion pathway for C_2H_6 and C_2H_4. From the concentration profiles in **Cage B** and **Cage A** along **Channel I**, it can be suspected that **Cage B** provides space for high adsorption capacity, while **Cage A** is a diffusion-limiting single-molecule passage, which may be the site to promote the kinetic selectivity of C_2H_6 over C_2H_4.

Given the essential role of **Cage A** in selective adsorption, the following MD simulations were performed to probe the free diffusion of gas molecules into **Cage A**. Ten parallel 500 ps MD simulations were carried out by modeling a discrete **Cage A** in the middle of a box filled with a C_2H_6/C_2H_4 (1 : 1) mixture that was randomly generated and annealed. As shown in Fig. 4, in 9 out of 10 simulations, it was the C_2H_6 molecule that diffused into **Cage A** and remained in it until the end of the 500 ps simulation. In the only simulation where the C_2H_4 molecule diffused into **Cage A**, it was, later on, exchanged out by the C_2H_6 molecule at 380 ps. The results reveal that **Cage A** is indeed a single-molecule passage

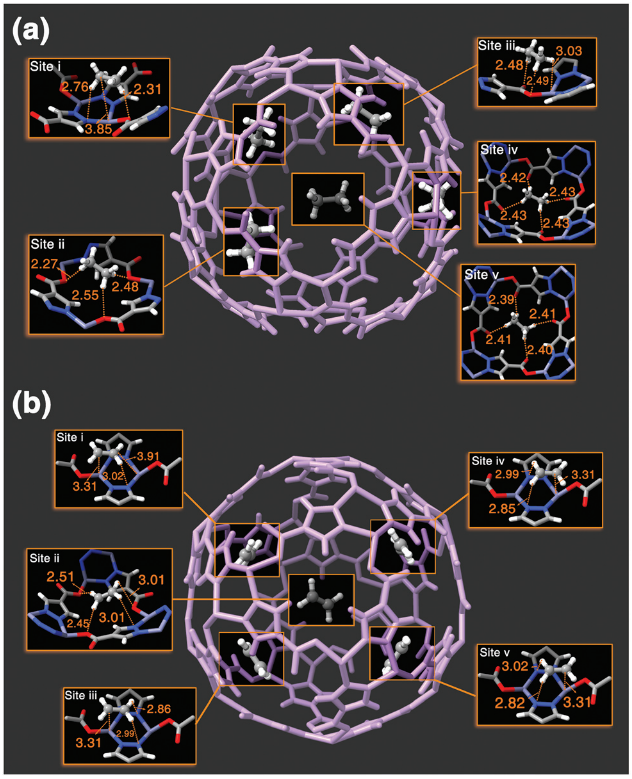

Fig. 5 The interaction configurations of (a) $5C_2H_6$@**Cage B** and (b) $5C_2H_4$@**Cage B**; all adsorption sites are highlighted and distances are in Å.

that can preferentially take in the C_2H_6 molecule, which is consistent with our speculation that **Cage A** is the origin of the kinetic selectivity.

DFT calculations

To quantify the host–guest interaction between adsorbate molecules and **JNU-2** and further elucidate the C_2H_6/C_2H_4 selective adsorption mechanism, we first performed DFT calculations on discrete **Cage B** with random addition of C_2H_6 or C_2H_4 molecules one by one. Five C_2H_6 or C_2H_4 molecules were introduced successfully, and their optimized conformations inside **Cage B** ($5C_2H_6$@**Cage B** and $5C_2H_4$@**Cage B**) are shown in Fig. 5. For the five C_2H_6 molecules in **Cage B**, two are at **Window 1** (site iv and v), two are close to **Window 2** (site ii and iii), and one is hovering over a carboxyl group (site i). All five C_2H_6 molecules interact with **Cage B** by forming multiple C–H⋯O interactions. In the case of $5C_2H_4$@**Cage B**, four C_2H_4 molecules are located nearby the Zn metal, forming weak metal-π-complexation with an interaction distance of about 3.3 Å, and the last one lies above **Window 2** (site ii). The interaction mode and adsorption sites for C_2H_6 molecules inside **Cage B** are rather different from C_2H_4 molecules, indicating that these two gas molecules do not necessarily compete for adsorption sites inside **Cage B**. The total interaction energy was calculated to be −30.97 kcal mol^{-1} for C_2H_6 and −32.11 kcal mol^{-1} for C_2H_4, which can be broken down into electrostatic interaction, Pauli repulsion, orbital interaction, and dispersion items based on energy decomposition analysis (EDA) (Table S1†). Although the electrostatic energy of $5C_2H_4$@**Cage B** appears to be higher, which can be attributed to the interaction between the π-electrons of C_2H_4 and metal cations, the overall adsorptions of C_2H_4 and C_2H_6 in **Cage B** are not much different in terms of thermodynamics. The results suggest that **Cage B** is the chamber for large adsorption, and may not be accountable for the selectivity of C_2H_6 over C_2H_4.

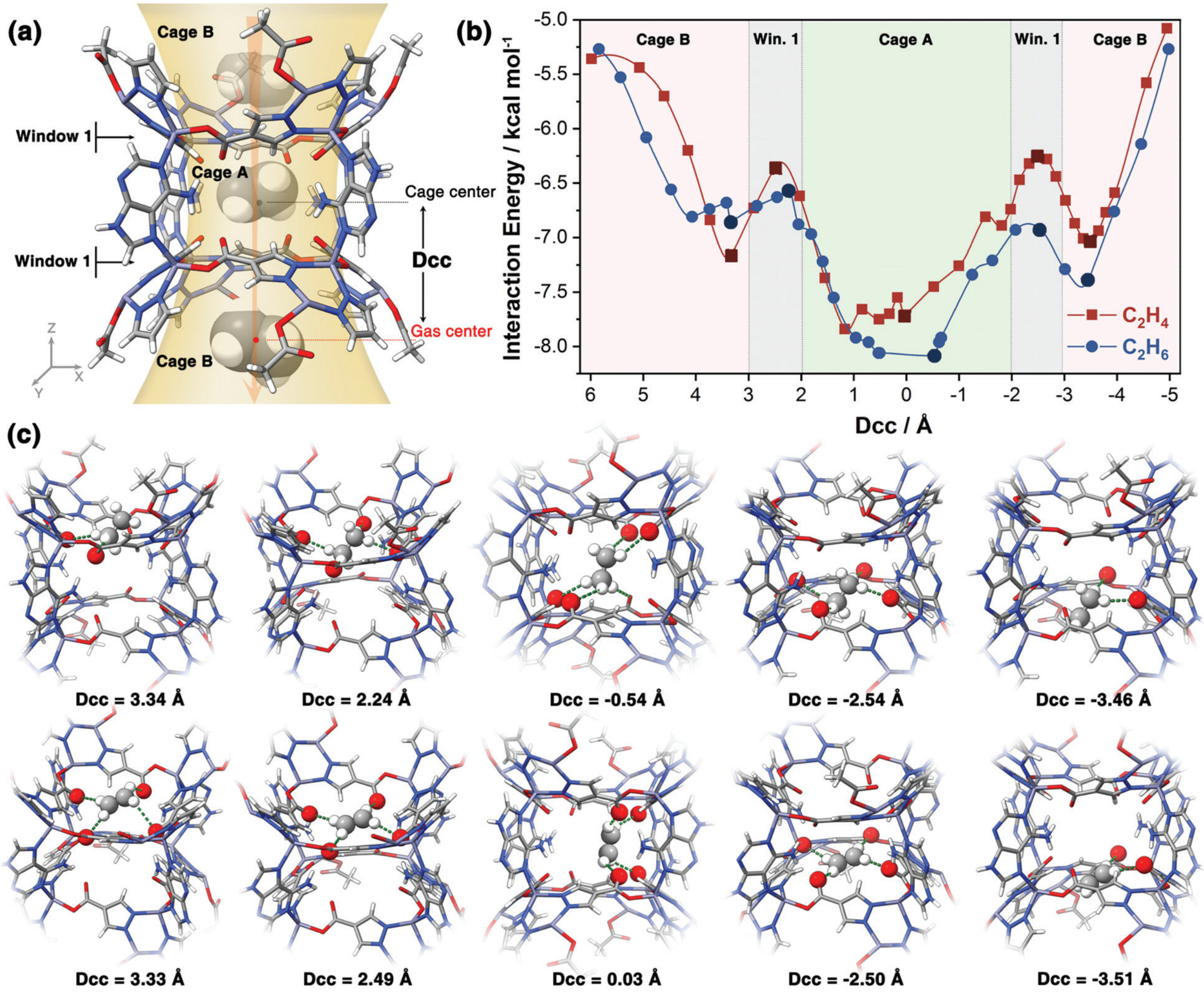

Fig. 6 (a) The model of **Cage A** with partial **Cage B** on both ends for DFT calculation and the definition of D_{cc}. (b) The interaction energy profile of gas molecules moving along the axis of D_{cc}. D_{cc} is displayed as negative when gas molecules are moving away from the center of **Cage A**. (c) The representative interaction configurations of C_2H_6@**Cage A** (top) and C_2H_4@**Cage A** (bottom); hydrogen bonds are labelled with green dashed lines.

To simulate the dynamic behavior of C_2H_6 and C_2H_4 in **Cage A**, we built a model of complete **Cage A** with parts of connecting **Cage B** and **Cage C**. Relaxed scanning was performed to produce a potential energy curve (PEV) of adsorbate molecules entering (from **Cage B** to **Cage A**) and exiting (from **Cage A** to **Cage B**) **Cage A** (see Fig. 6a). The corresponding interaction energies between adsorbate molecules and **JNU-2** and PEV at each configuration point were calculated and depicted in Fig. 6b and S10.†

The whole process of the C_2H_6/C_2H_4 molecule passing through **Cage A** can be divided into five stages: **Cage B** edge, **Window 1**, **Cage A**, **Window 1**, and **Cage B** edge. The calculated interaction energies vary from −5.0 to −8.0 kcal mol^{-1}, indicating an energetically favourable pathway for both C_2H_6 and C_2H_4 (Fig. 6b). In detail, the overall interaction energy shows a trough-like curve with an obvious barrier at **Window 1**, which can be attributed to steric hindrance and electrostatic repulsion at the narrowest part of **Window 1**. The representative interaction configurations (Fig. 6c) show that the C_2H_6 molecule enters and exits **Cage A** smoothly with some molecular rotation along the movement path. Except on the **Cage B** edge, the C_2H_6 molecule maintains at least four weak hydrogen bonds with **Cage A** throughout the entire entering and exiting process. At the center of **Cage A** (D_{cc} = −0.54 Å, Fig. 6c), C_2H_6 is in a diagonal-like configuration and interacts with heteroatoms on both **Window 1**, resulting in five hydrogen bonds in total. As for C_2H_4, the energy barrier at **Window 1** is relatively larger, indicating that it is less favourable for C_2H_4 to enter into **Cage A**, which is consistent with the MD simulations. In addition, the C_2H_4 molecule does not pass through **Cage A** in a parallel configuration (Fig. 6c and Fig. S12†). A flip was observed for the C_2H_4 molecule to turn to the side of **Cage A** and maintain four hydrogen-bonding interactions. Even so, the interaction between C_2H_4 and **Cage A** is weaker than that between C_2H_6 and **Cage A** at its center.

Overall, **Cage A** is a single-molecule passage for gas molecules to enter into **Cage B**, which is a gas storage chamber accounting for the large adsorption of C_2H_6 and C_2H_4. C_2H_6 can maintain a steady configuration and strong interaction throughout the whole diffusion process, especially at the center of **Cage A**. However, C_2H_4 has to adjust its molecular configuration to maintain strong interaction with **Cage A**, resulting in a less favourable interaction pathway for C_2H_4 entering and exiting **Cage A**. It should be pointed out that the gas molecule has to enter **Cage A** to reach **Cage B**; considering the fact that the possibility of C_2H_6 entering into **Cage A** is 9 times higher than that of C_2H_4, a kinetic selectivity of C_2H_6 over C_2H_4 can thus be rationalized by the multi-scale simulation study.

Conclusions

In summary, we carried out a multi-scale simulation study on **JNU-2** to explore its adsorption and separation behaviour of C_2H_6 and C_2H_4. The results justify a C_2H_6-favoured kinetic separation mechanism that has rarely been observed in adsorption separation in porous materials. The adsorption isotherms obtained from GCMC simulations on **JNU-2** with **Cage C** blocked are consistent with the experimental ones, suggesting that these gas molecules are only adsorbed in the two smaller cages (**Cage A** and **Cage B**). MD simulations confirm that the only gas diffusion channel is the one (**Channel I**) that connects **Cage A** and **Cage B**, and the probability of C_2H_6 diffusing into **Cage A** is 9 times higher than that of C_2H_4. DFT calculations further clarify that **Cage B** provides space for large adsorption of both C_2H_6 and C_2H_4 with little difference in terms of adsorption heat and no competition for strong adsorption sites. Meanwhile, the single-molecule passage **Cage A** can provide multiple hydrogen-bonding interactions with both C_2H_6 and C_2H_4, and the overall energy diagram turns out to be more conducive to the adsorption and diffusion of C_2H_6, resulting in a kinetic selectivity of C_2H_6 over C_2H_4. This work successfully illustrated the underlying kinetic separation mechanism of C_2H_6 over C_2H_4 on **JNU-2** by adopting multi-scale simulations, demonstrating a new kinetic separation mechanism of interaction screening and providing an effective theoretical methodology for better understanding the gas adsorption and separation in MOFs.

Computational details

GCMC simulation

Grand Canonical Monte Carlo (GCMC) calculations were performed with the Sorption module embedded in Materials Studio 2018 and RASPA 2.0[23] to simulate the C_2H_6/C_2H_4 adsorption properties of **JNU-2**. In GCMC simulations, the **JNU-2** structure was taken from the experimental crystallographic data in our previous work, and the conventional cubic unit cell of **JNU-2** ($a = b = c = 43.55$ Å, $\alpha = \beta = \gamma = 90°$) was utilized; the periodic boundary conditions were applied in all the three directions. The **JNU-2** structure was kept rigid by constructing the atoms in the **JNU-2** structure in simulations. All GCMC simulations including 2.5×10^6 equilibration cycles followed by 2.5×10^6 production cycles were carried out at 298 K and various pressure points from 0.01 bar to 1.0 bar. The intermolecular interactions were represented using a Lennard-Jones (LJ) potential which is defined as follows:

The LJ parameters for atoms in **JNU-2** were all taken from the universal force field (UFF),[24–26] and the LJ parameters for ethane and ethylene were taken from the TraPPE force field.[27–29] The combined UFF/TraPPE force field is widely used to predict adsorption properties in the MOF research field.[30] The Lorentz–Berthelot mixing rules[31] were applied in describing the cross interactions between different atom types. The Ewald summation was used to calculate the electrostatic interactions. The charge equilibration (Q_{eq}) method[32] was applied to compute the atomic partial charges for **JNU-2**, and the atomic charges for methane/ethylene were calculated by employing the density functional theory (DFT) at the B3LYP[33]/def2-TZVP[34] theoretical level. Table S2† lists the atomic charges of methane and ethylene. A cutoff of 12.5 Å in the interaction distance was used in all GCMC simulations.

Pore volume and window diameter analysis

The isolated cage structures of **Cage A**, **B**, and **C** were intercepted from the crystal structure of **JNU-2**. The cavity volumes of the cages were estimated using the VIODOO program[35] using a 2.8 Å probe radius. **Cage A** was visualized by using the ChimeraX 1.0 program.[36] The cross-sections of the accessible volume and the window position of each cage were made by utilizing the "slab" tool in ChimeraX, so that the window size could be obtained.

MD simulation

The simulation models are composed of a mixed gas layer, framework layer, and vacuum layer. The z-direction of the triclinic simulation box ($\alpha = \beta = \gamma = 90°$) is fixed to 200 Å. The framework layers are cleaved from the crystal structure of **JNU-2** including at least one group of adjacent cavities in each channel. The size of the framework layer along the z-direction is controlled at about 50 Å. The broken chemical bonds in the cleaved surface are saturated with hydrogen or methyl. The two frame layers on both sides are surface symmetrical so that the two interfaces in contact with the gas molecules are the same. The mixed gas layers are set to be about 50 Å in the z-direction and randomly filled with C_2H_6 and C_2H_4 molecules with the same molar ratio maintaining the gas densities in the three models at about 0.08 g cm^{-3}. The vacuum layers on both sides are set to be about 25 Å in the z-direction. Periodic boundary conditions (PBC) are applied in the x- and y-directions, so that the gas molecules can diffuse along the z-direction into the framework layer and finally reach the vacuum layer in the presence of the gas pressure difference.

In MD simulations, a flexible **JNU-2** model was adopted for the framework layer. The structural parameter of the UFF4MOF force field[25,26] was used for Cu and Zn ions, which was specially made for MOFs, while the other atoms of **JNU-2** adopting the UFF force field and the TraPPE force field was used for C_2H_6 and C_2H_4. The charge calculation and equilibration method here was consistent with the GCMC simulation. The Lorentz–Berthelot combination rules were applied to obtain the LJ cross potential parameters for intermolecular interactions. The Ewald summation was used to calculate the electrostatic interactions. In addition, a discrete **Cage A** structure from **JNU-2** was placed at the center of a box (30 Å × 30 Å × 30 Å) filled with a C_2H_6/C_2H_4 (1 : 1) mixture that was randomly generated and annealed. Ten parallel 500 ps MD simulations were carried out by employing the same parameters as above.

All the MD simulations were performed with the Forcite module in the Materials Studio 2018 program. The framework layers were first optimized to a convergence tolerance of an energy difference less than 0.001 kcal mol^{-1} and force less than 0.5 kcal mol^{-1} $Å^{-1}$. The mixed gas molecules are then added into the mixed gas layer in the middle of the simulation box. Three-channel models were simulated for 20 ns with a time step of 2.0 fs using a canonical ensemble (NVT) with an Anderson thermostat at 298 K. The concentrations of gas molecules in all three models were analyzed based on the trajectory of MD simulation in the specified x-, y- and z-directions.

DFT calculations

Density functional theory (DFT) calculations were performed to assess the behavior of gas adsorption in **Cage B** and energy changes of C_2H_4 and C_2H_6 when passing through **Cage A**. The cluster models of **Cage A** and **Cage B** used in DFT calculations were taken from the crystal structure of **JNU-2**; the truncated chemical bonds were saturated with hydrogen or methyl. The **Cage B**–absorbate interaction model was constructed by fixing the geometry of **Cage B** and randomly adding the gas molecules one by one, and the final interaction configurations were obtained by optimization. As for **Cage A**, we conducted a relaxed potential surface scanning on the energy of the gas crossing process using modredundant calculations. The distance between the center of the gas molecule and the center of **Cage A** (D_{cc}) was set as the scan variable, making the gas molecule move along the z-axis and optimize the structure of the gas molecule and calculate the energy, so that the whole crossing process, *i.e.* **Cage B** – **Window 1** – **Cage A** – **Window 1** – **Cage B**, was included in the scanning. Furthermore, we calculated the interaction energies between the gas molecule and **Cage A** in each scanning step and the basis set superposition error (BSSE) was considered herein. Optimization and energy calculations were performed using Gaussian09 program[37] employing the B3LYP functional[33] with Grimme's dispersion correction[38–40] (B3LYP–D3(BJ)). The effective core potential LanL2DZ[41] and the corresponding basis set were used for the Zn and Cu atom, and the double zeta basis set 6-31G(d)[42] was used for other atoms. The energy decomposition analysis (EDA)[43] calculations were performed using Amsterdam Density Functional (ADF) 2019 suit of the program[44] at the B3LYP–D3 (BJ)/TZP theoretical level without a frozen core. The EDA scheme divides the total interaction energy into the following items:

$$\Delta E_{\text{tot}} = \Delta E_{\text{ele}} + \Delta E_{\text{rep}} + \Delta E_{\text{orb}} + \Delta E_{\text{disp}}$$

where ele, rep, orb, and disp denote the electrostatic interaction, Pauli repulsion, orbital interaction, and dispersion, respectively.

Author contributions

M. Xie and Z. Lu performed all calculations, data curation, and visualization and wrote the original draft. M. Xie and W. Lu conceived and conceptualized the research. W. Lu and D. Li supervised the research and reviewed and polished the manuscript.

Conflicts of interest

There are no conflicts to declare.

Acknowledgements

This work was financially supported by the National Natural Science Foundation of China (No. 21731002, 21975104, 22150004, and 22101099), the Guangdong Major Project of Basic and Applied Research (No. 2019B030302009), and the Guangdong Basic and Applied Basic Research Foundation (No. 2020A1515011005). We thank the high-performance public computing service platform of Jinan University for providing computational resources. We also appreciate Xiao-Jing Xie (Jinan University) and Dr. Weijie Zhang (Univ. of North Texas) for their help and discussion.

Notes and references

1 J.-R. Li, J. Sculley and H.-C. Zhou, Metal–Organic Frameworks for Separations, *Chem. Rev.*, 2012, **112**, 869–932.

2 K. Sumida, D. L. Rogow, J. A. Mason, T. M. McDonald, E. D. Bloch, Z. R. Herm, T.-H. Bae and J. R. Long, Carbon Dioxide Capture in Metal–Organic Frameworks, *Chem. Rev.*, 2012, **112**, 724–781.

3 Y. He, W. Zhou, G. Qian and B. Chen, Methane Storage in Metal–Organic Frameworks, *Chem. Soc. Rev.*, 2014, **43**, 5657–5678.

4 H. Furukawa, K. E. Cordova, M. O'Keeffe and O. M. Yaghi, The Chemistry and Applications of Metal-Organic Frameworks, *Science*, 2013, **341**, 1230444.

5 W.-G. Cui, T.-L. Hu and X.-H. Bu, Metal–Organic Framework Materials for the Separation and Purification of Light Hydrocarbons, *Adv. Mater.*, 2020, **32**, 1806445.

6 R.-B. Lin, S. Xiang, W. Zhou and B. Chen, Microporous Metal-Organic Framework Materials for Gas Separation, *Chem*, 2020, **6**, 337–363.

7 A. J. Rieth, A. M. Wright and M. Dincă, Kinetic Stability of Metal–Organic Frameworks for Corrosive and Coordinating Gas Capture, *Nat. Rev. Mater.*, 2019, **4**, 708–725.

8 H. Zeng, M. Xie, T. Wang, R.-J. Wei, X.-J. Xie, Y. Zhao, W. Lu and D. Li, Orthogonal-Array Dynamic Molecular Sieving of Propylene/Propane Mixtures, *Nature*, 2021, **595**, 542–548.

9 J.-R. Li, R. J. Kuppler and H.-C. Zhou, Selective Gas Adsorption and Separation in Metal–Organic Frameworks, *Chem. Soc. Rev.*, 2009, **38**, 1477–1504.

10 L. Yang, S. Qian, X. Wang, X. Cui, B. Chen and H. Xing, Energy-Efficient Separation Alternatives: Metal–Organic Frameworks and Membranes for Hydrocarbon Separation, *Chem. Soc. Rev.*, 2020, **49**, 5359–5406.

11 Ü. Kökçam-Demir, A. Goldman, L. Esrafili, M. Gharib, A. Morsali, O. Weingart and C. Janiak, Coordinatively Unsaturated Metal Sites (Open Metal Sites) in Metal–Organic Frameworks: Design and Applications, *Chem. Soc. Rev.*, 2020, **49**, 2751–2798.

12 E. D. Bloch, W. L. Queen, R. Krishna, J. M. Zadrozny, C. M. Brown and J. R. Long, Hydrocarbon Separations in a Metal-Organic Framework with Open Iron(II) Coordination Sites, *Science*, 2012, **335**, 1606–1610.

13 R.-B. Lin, L. Li, H.-L. Zhou, H. Wu, C. He, S. Li, R. Krishna, J. Li, W. Zhou and B. Chen, Molecular Sieving of Ethylene from Ethane Using a Rigid Metal–Organic Framework, *Nat. Mater.*, 2018, **17**, 1128–1133.

14 D.-D. Zhou, P. Chen, C. Wang, S.-S. Wang, Y. Du, H. Yan, Z.-M. Ye, C.-T. He, R.-K. Huang, Z.-W. Mo, N.-Y. Huang and J.-P. Zhang, Intermediate-Sized Molecular Sieving of Styrene from Larger and Smaller Analogues, *Nat. Mater.*, 2019, **18**, 994–998.

15 A. L. Dzubak, L.-C. Lin, J. Kim, J. A. Swisher, R. Poloni, S. N. Maximoff, B. Smit and L. Gagliardi, Ab initio Carbon Capture in Open-Site Metal–Organic Frameworks, *Nat. Chem.*, 2012, **4**, 810–816.

16 W. Chen, L. Huang, X. Yi and A. Zheng, Lithium Doping on 2D Squaraine-Bridged Covalent Organic Polymers for Enhancing Adsorption Properties: a Theoretical Study, *Phys. Chem. Chem. Phys.*, 2018, **20**, 6487–6499.

17 D. J. Vogel, J. M. Rimsza and T. M. Nenoff, Prediction of Reactive Nitrous Acid Formation in Rare–Earth MOFs via ab initio Molecular Dynamics, *Angew. Chem., Int. Ed.*, 2021, **60**, 11514–11522.

18 Y. Ying, Z. Zhang, S. B. Peh, A. Karmakar, Y. Cheng, J. Zhang, L. Xi, C. Boothroyd, Y. M. Lam, C. Zhong and D. Zhao, Pressure–Responsive Two-Dimensional Metal–Organic Framework Composite Membranes for CO_2 Separation, *Angew. Chem., Int. Ed.*, 2021, **60**, 11318–11325.

19 W.-Q. Lin, X.-L. Xiong, H. Liang and G.-H. Chen, Multiscale Computational Screening of Metal–Organic Frameworks for Kr/Xe Adsorption Separation: A Structure–Property Relationship-Based Screening Strategy, *ACS Appl. Mater. Interfaces*, 2021, **13**, 17998–18009.

20 H. Zeng, X.-J. Xie, M. Xie, Y.-L. Huang, D. Luo, T. Wang, Y. Zhao, W. Lu and D. Li, Cage-Interconnected Metal–Organic Framework with Tailored Apertures for Efficient C_2H_6/C_2H_4 Separation under Humid Conditions, *J. Am. Chem. Soc.*, 2019, **141**, 20390–20396.

21 S. L. Mayo, B. D. Olafson and W. A. Goddard, DREIDING: A Generic Force Field for Molecular Simulations, *J. Phys. Chem.*, 1990, **94**, 8897–8909.

22 W. L. Jorgensen, D. S. Maxwell and J. Tirado-Rives, Development and Testing of the OPLS All-Atom Force Field on Conformational Energetics and Properties of Organic Liquids, *J. Am. Chem. Soc.*, 1996, **118**, 11225–11236.

23 D. Dubbeldam, S. Calero, D. E. Ellis and R. Q. Snurr, RASPA: Molecular Simulation Software for Adsorption and Diffusion in Flexible Nanoporous Materials, *Mol. Simul.*, 2016, **42**, 81–101.

24 A. K. Rappe, C. J. Casewit, K. S. Colwell, W. A. Goddard and W. M. Skiff, UFF, a Full Periodic Table Force Field for

Molecular Mechanics and Molecular Dynamics Simulations, *J. Am. Chem. Soc.*, 1992, **114**, 10024–10035.

25 M. A. Addicoat, N. Vankova, I. F. Akter and T. Heine, Extension of the Universal Force Field to Metal–Organic Frameworks, *J. Chem. Theory Comput.*, 2014, **10**, 880–891.

26 D. E. Coupry, M. A. Addicoat and T. Heine, Extension of the Universal Force Field for Metal–Organic Frameworks, *J. Chem. Theory Comput.*, 2016, **12**, 5215–5225.

27 B. Chen and J. I. Siepmann, Transferable Potentials for Phase Equilibria. 3. Explicit-Hydrogen Description of Normal Alkanes, *J. Phys. Chem. B*, 1999, **103**, 5370–5379.

28 M. G. Martin and J. I. Siepmann, Transferable Potentials for Phase Equilibria. 1. United-Atom Description of n-Alkanes, *J. Phys. Chem. B*, 1998, **102**, 2569–2577.

29 C. D. Wick, M. G. Martin and J. I. Siepmann, Transferable Potentials for Phase Equilibria. 4. United-Atom Description of Linear and Branched Alkenes and Alkylbenzenes, *J. Phys. Chem. B*, 2000, **104**, 8008–8016.

30 J. G. McDaniel, S. Li, E. Tylianakis, R. Q. Snurr and J. R. Schmidt, Evaluation of Force Field Performance for High-Throughput Screening of Gas Uptake in Metal–Organic Frameworks, *J. Phys. Chem. C*, 2015, **119**, 3143–3152.

31 C. L. Kong, Combining Rules for Intermolecular Potential Parameters. II. Rules for the Lennard-Jones (12–6) Potential and the Morse Potential, *J. Chem. Phys.*, 1973, **59**, 2464–2467.

32 A. K. Rappe and W. A. Goddard, Charge Equilibration for Molecular Dynamics Simulations, *J. Phys. Chem.*, 1991, **95**, 3358–3363.

33 A. D. Becke, Density–Functional Thermochemistry. III. The Role of Exact Exchange, *J. Chem. Phys.*, 1993, **98**, 5648–5652.

34 F. Weigend, Accurate Coulomb-Fitting Basis Sets for H to Rn, *Phys. Chem. Chem. Phys.*, 2006, **8**, 1057–1065.

35 G. J. Kleywegt and T. A. Jones, Detection, Delineation, Measurement and Display of Cavities in Macromolecular Structures, *Acta Crystallogr., Sect. D: Biol. Crystallogr.*, 1994, **50**, 178–185.

36 T. D. Goddard, C. C. Huang, E. C. Meng, E. F. Pettersen, G. S. Couch, J. H. Morris and T. E. Ferrin, UCSF ChimeraX: Meeting Modern Challenges in Visualization and Analysis, *Protein Sci.*, 2018, **27**, 14–25.

37 G. W. Trucks, M. J. Frisch, H. B. Schlegel, G. E. Scuseria, M. A. Robb, J. R. Cheeseman, G. Scalmani, V. Barone, B. Mennucci, G. A. Petersson, H. Nakatsuji, M. Caricato, X. Li, H. P. Hratchian, A. F. Izmaylov, J. Bloino, G. Zheng, J. L. Sonnenberg, M. Hada, M. Ehara, K. Toyota, R. Fukuda, J. Hasegawa, M. Ishida, T. Nakajima, Y. Honda, O. Kitao, H. Nakai, T. Vreven, J. A. Montgomery Jr., J. E. Peralta, F. Ogliaro, M. Bearpark, J. J. Heyd, E. Brothers, K. N. Kudin, V. N. Staroverov, R. Kobayashi, J. Normand, K. Raghavachari, A. Rendell, J. C. Burant, S. S. Iyengar, J. Tomasi, M. Cossi, N. Rega, J. M. Millam, M. Klene, J. E. Knox, J. B. Cross, V. Bakken, C. Adamo, J. Jaramillo, R. Gomperts, R. E. Stratmann, O. Yazyev, A. J. Austin, R. Cammi, C. Pomelli, J. W. Ochterski, R. L. Martin, K. Morokuma, V. G. Zakrzewski, G. A. Voth, P. Salvador, J. J. Dannenberg, S. Dapprich, A. D. Daniels, Ö. Farkas, J. B. Foresman, J. V. Ortiz, J. Cioslowski and D. J. Fox, *Gaussian* 09, Inc., Wallingford CT, 2009.

38 S. Grimme, J. Antony, S. Ehrlich and H. Krieg, A Consistent and Accurate ab initio Parametrization of Density Functional Dispersion Correction (DFT-D) for the 94 Elements H-Pu, *J. Chem. Phys.*, 2010, **132**, 154104.

39 S. Grimme, Accurate Description of van der Waals Complexes by Density Functional Theory Including Empirical Corrections, *J. Comput. Chem.*, 2004, **25**, 1463–1473.

40 S. Grimme, Semiempirical GGA-Type Density Functional Constructed with a Long-Range Dispersion Correction., *J. Comput. Chem.*, 2006, **27**, 1787–1799.

41 L. E. Roy, P. J. Hay and R. L. Martin, Revised Basis Sets for the LANL Effective Core Potentials, *J. Chem. Theory Comput.*, 2008, **4**, 1029–1031.

42 P. C. Hariharan and J. A. Pople, The Influence of Polarization Functions on Molecular Orbital Hydrogenation Energies, *Theor. Chim. Acta*, 1973, **28**, 213–222.

43 L. Zhao, M. von Hopffgarten, D. M. Andrada and G. Frenking, Energy Decomposition Analysis, *Wiley Interdiscip. Rev.: Comput. Mol. Sci.*, 2017, **8**, e1345.

44 T. Ziegler, E. J. Baerends, J. Autschbach, D. Bashford, A. Bérces, F. M. Bickelhaupt, C. Bo, P. M. Boerrigter, L. Cavallo, D. P. Chong, L. Deng, R. M. Dickson, D. E. Ellis, M. van Faassen, L. Fan, T. H. Fischer, C. Fonseca Guerra, M. Franchini, A. Ghysels, A. Giammona, S. J. A. van Gisbergen, A. W. Götz, J. A. Groeneveld, O. V. Gritsenko, M. Grüning, S. Gusarov, F. E. Harris, P. van den Hoek, C. R. Jacob, H. Jacobsen, L. Jensen, J. W. Kaminski, G. van Kessel, F. Kootstra, A. Kovalenko, M. V. Krykunov, E. van Lenthe, D. A. McCormack, A. Michalak, M. Mitoraj, S. M. Morton, J. Neugebauer, V. P. Nicu, L. Noodleman, V. P. Osinga, S. Patchkovskii, M. Pavanello, P. H. T. Philipsen, D. Post, C. C. Pye, W. Ravenek, J. I. Rodríguez, P. Ros, P. R. T. Schipper, H. van Schoot, G. Schreckenbach, J. S. Seldenthuis, M. Seth, J. G. Snijders, M. Solà, M. Swart, D. Swerhone, G. te Velde, P. Vernooijs, L. Versluis, L. Visscher, O. Visser, F. Wang, T. A. Wesolowski, E. M. van Wezenbeek, G. Wiesenekker, S. K. Wolff, T. K. Woo and A. L. Yakovlev, *ADF*, 2018, SCM, Theoretical Chemistry, Vrije Universiteit, Amsterdam, The Netherlands, URL:**https://www.scm.com**.